

An Adaptive Correspondence Scoring Framework for Unsupervised Image Registration of Medical Images

Xiaoran Zhang
Yale University

xiaoran.zhang@yale.edu

John C. Stendahl
Yale University

john.stendahl@yale.edu

Lawrence Staib
Yale University

lawrence.staib@yale.edu

Albert J. Sinusas
Yale University

albert.sinusas@yale.edu

Alex Wong
Yale Vision Lab

alex.wong@yale.edu

James S. Duncan
Yale University

james.duncan@yale.edu

Abstract

*We propose an adaptive training scheme for unsupervised medical image registration. Existing methods rely on image reconstruction as the primary supervision signal. However, nuisance variables (e.g. noise and covisibility) often cause the loss of correspondence between medical images, violating the Lambertian assumption in physical waves (e.g. ultrasound) and consistent imaging acquisition. As the unsupervised learning scheme relies on intensity constancy to establish correspondence between images for reconstruction, this introduces spurious error residuals that are not modeled by the typical training objective. To mitigate this, we propose an adaptive framework that reweights the error residuals with a correspondence scoring map during training, preventing the parametric displacement estimator from drifting away due to noisy gradients, which leads to performance degradations. To illustrate the versatility and effectiveness of our method, we tested our framework on three representative registration architectures across three medical image datasets along with other baselines. Our proposed adaptive framework consistently outperforms other methods both quantitatively and qualitatively. Paired *t*-tests show that our improvements are statistically significant. The code will be publicly available at <https://voldemort108x.github.io/AdaCS/>.*

1. Introduction

Deformable medical image registration aims to accurately determine non-rigid correspondences through dense displacement vectors between a source image and a target image. This process is a crucial step for medical image analysis, such as tracking disease progression for diagnosis and treatment [12, 26]. Due to the impracticality of

obtaining ground truth displacement, it has been a long-standing problem and is extensively studied in the past decades [1, 4, 7, 20, 21, 28, 34].

Classical methods approach this challenge by solving an iterative pair-wise optimization problem between source and target images using elastic-type models [10, 21], free-form deformations with b-splines [28], and topology-preserving diffeomorphic models [1, 2]. However, these approaches are computationally expensive and time-consuming, limiting their practical utility in large-scale real-world data. Recently, learning-based approaches have been extensively studied to address this challenge with state-of-the-art performance [4, 7, 8, 20, 30, 34]. These approaches formulate displacement estimation as a generative modeling process from query source-target pair and operate under an unsupervised setting or a weakly supervised setting with segmentation masks due to the lack of ground truth displacement. To train these approaches via gradient-based optimization, image reconstruction from a source to a target serves as a data fidelity term. The supervision signal comes from minimizing the reconstruction error between warped source and target. The feasibility in minimizing this term relies on intensity constancy between the two images during imaging, along with a regularization term based on the assumption that the object imaged is locally smooth and connected.

However, assuming such intensity constancy uniformly across the entire image domain neglects the fact of motion ambiguity and non-uniform noise corruption in medical images. Assuming sufficiently exciting local regions, only a subset of pixels of one image can be uniquely matched or corresponded to another based on the image intensity profiles. As shown in Fig. 1, despite a displacement estimator model predicting largely correct corresponding pixels between the two images, the error residuals between the warped source and target images are still non-zero. In fact, they are dominated by regions with no correspondence; when

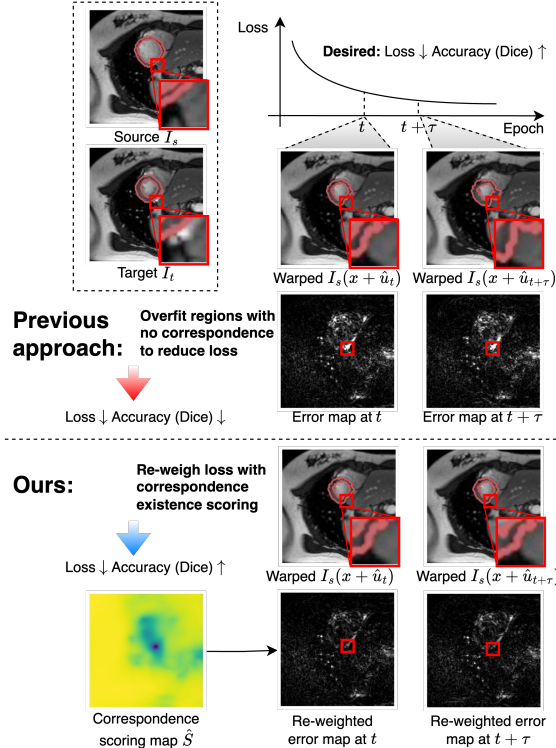


Figure 1. The previous approach assumes uniform intensity constancy across the entire image, causing overfitting during training in regions with large error residuals due to the absence of correspondence as highlighted in the red box. Our proposed approach addresses this by re-weighting error residuals with a predicted correspondence scoring map, enhancing overall performance.

this phenomenon occurs during the training of a displacement estimator, it results in performance degradation (driven towards an undesirable minimum) in the subsequent optimization steps due to the noisy gradients. To address this issue, we propose a self-supervised correspondence scoring framework that identifies regions with high chance of establishing correspondence and adaptively reduces the influence of error residuals from nuisance variability during training, preventing the displacement estimator from drifting away due to large residuals caused by the lack of correspondence between input image pairs.

Our proposed scoring estimator is deployed during the unsupervised training of a displacement estimator and yields a soft map. It is optimized alternately together with the displacement estimator to adaptively re-weight the data-fidelity term in order to mitigate the negative impact of nuisances when establishing correspondence. We introduce a self-supervised strategy for the scoring estimator to learn an accurate correspondence scoring map without additional annotation. Yet, there exists a trivial solution of all zeros. Therefore, we additionally propose a regularizer for the scoring estimator to bias it away from the trivial solution, along

with a momentum-guided adaptive total variation to encourage smoothness in the scoring map. To validate the effectiveness of our proposed method, we tested on three different datasets including: 1) ACDC (public 2D MRI) [5] 2) CAMUS (public 2D ultrasound) [22] and 3) private 3D echocardiography. To further show the versatility of our proposed method, we tested on three representative unsupervised image registration architectures including: 1) Voxelmorph [4], 2) Transmorph [7] and 3) Diffusemorph [20] along with other baselines. Our proposed framework can be applied in a plug-and-play manner to consistently improve existing methods. Paired t-tests show that the improvement gains obtained by utilizing our approach are statistically significant.

Our contributions

- We propose an adaptive framework that incorporates correspondence scoring for unsupervised deformable medical image registration.
- We introduce a self-supervised correspondence scoring network to be used during the training of a displacement estimator. The scoring network learns to determine whether a given allows for establishing correspondence by minimizing the typical image reconstruction loss with scoring and momentum-guided adaptive regularization.
- We demonstrate that our proposed method consistently outperforms other baselines across three representative registration architectures over three medical image datasets with diverse modalities.
- The performance gain during inferences comes with no additional cost in memory or run time, but only the deployment of our scoring estimation during training.

2. Related works

2.1. Unsupervised medical image registration

Balakrishnan et al. [4] proposed an unsupervised learning framework using U-Net as the displacement estimator. This framework imposes intensity constancy by minimizing the mean squared error between the warped source image and the target image to update the parametric displacement estimator via gradient-based optimization. A number of works have been developed upon this architecture including adding diffeomorphic regularization (Voxelmorph-diff) [9], jointly learning amortized hyperparameters (Hypermorph) [16] and learning contrast-invariant registration without acquired images (SynthMorph) [13].

Inspired by the recent advances in vision transformers [11, 23], Chen et al. [7] introduced TransUNet [6], a hybrid Transformer-CNN architecture. This design replaces encoders with Swin Transformer [23] to enhance the receptive field while preserving convolutional decoders to bolster the model’s ability to capture long-range motion. A number of extensions to this architecture have been proposed, such as

substituting convolutional decoders with transformer layers [30] and incorporating multi-scale pyramids [24].

Additionally, score-based diffusion models such as DDPM [31] have shown high-quality performance in generative modeling. To leverage the advantage of DDPM, Kim et al. [20] presents a diffusion-based architecture, composed of a diffusion network and a deformation network. Recent work built upon this architecture explores adding feature and score-wise diffusion [27].

In this paper, we validated our proposed adaptive framework along with other related formulations as baselines on three representative architectures including: 1) Voxelmorph [4], 2) Transmorph [7] and 3) Diffusemorph [20].

2.2. Adaptive weighting schemes

A wide range of image processing problems involve optimizing an energy function that combines a data-fidelity term and a regularization term. The relative importance between the two terms is usually weighted by a scalar, which disregards the heteroscedastic nature of error residuals [33]. To address this challenge, several adaptive weighting schemes are proposed in the spatial domain and over the course of optimization based on the local residual [14, 15, 32]. Wong et al. [33] later provides a data-driven algorithm that deals with multiple frames [33]. In this paper, we selected AdaReg [32] and AdaFrame [33] as our baselines for adaptive weighting.

2.3. Aleatoric uncertainty estimation

Our proposed adaptive correspondence scoring is conceptually related to aleatoric uncertainty modeling in the Bayesian learning framework, which aims to estimate input-dependent noise inherent in the observations [3, 17, 19, 25, 29]. This can be attributed to for example motion noise or sensor noise, resulting in uncertainty which cannot be reduced even if more data were to be collected. Kendall and Gal [19] proposed a maximum likelihood estimation (MLE) formulation that minimizes the negative log-likelihood (NLL) criterion using stochastic gradient descent. This approach re-weights the data fidelity term using predictive variance estimates mediated by a regularization term after assuming noise distribution is heteroscedastic Gaussian. Seitzer et al. [29] later identifies that such formulation using inverse variance weighting will result in over-confident of variance estimates, leading to undesired undersampling. Thus, an exponentiated β term is proposed in the new loss formulation, termed β -NLL, to counteract the undersampling leading to undesired performance. In this paper, we selected NLL [19] and β -NLL [29] as baselines for aleatoric uncertainty estimation with a U-Net based variance estimator that is jointly trained with displacement estimator under each formulation.

3. Preliminary

Let I_s be the source image and I_t be the target image, where $I : \Omega \rightarrow [0, 1]$ is the imaging functions after normalization and Ω is the image space. Unsupervised deformable image registration aims to estimate a dense displacement vector field that characterizes the correspondence between two images for each pixel $\hat{u} : \Omega \rightarrow \mathbb{R}^2$.

Due to the lack of ground truth, intensity constancy and the smoothness assumption are imposed to supervise the parametric model $f_\theta(\cdot)$ (e.g. a neural network) as displacement estimator $\hat{u} = f_\theta(I_t, I_s)$ by minimizing the following objective to update the parameters θ in the model

$$\mathcal{L} = \frac{1}{|\Omega|} \sum_{x \in \Omega} \underbrace{\|I_t(x) - I_s(x + \hat{u}(x))\|_2^2}_{\mathcal{L}_{\text{data}}} + \lambda \|\nabla \hat{u}(x)\|_2^2, \quad (1)$$

where $x \in \Omega$ denotes a coordinate and the λ a hyperparameter model the trade-off between two terms. In this work, we explore three representative deep neural network architectures that serve as displacement estimators including 1) convolution-based (Voxelmorph [4]), 2) transformer-based (Transmorph [7]) and 3) diffusion-based (Diffusemorph [20]).

4. Methods

4.1. Adaptive displacement estimation

To train these networks in an unsupervised fashion, one typically minimizes Eq. (1) with respect to the model parameters. However, the data term $\mathcal{L}_{\text{data}}$, which measures the intensity difference between two estimated correspondences, relies on intensity constancy and assumes that surfaces reflecting the physical waves (i.e., ultrasound) are largely Lambertian [18] and the acquisition techniques are consistent – in which case, one can determine unique correspondences between two images, if they are covisible. In the case where the corresponding pixel is *not covisible*, then the solution cannot be uniquely determined and one must rely on the regularizer, i.e., local smoothness. Under realistic scenarios, the Lambertian assumption is often violated and the difficulty of establishing unique correspondences is further exacerbated by the presence of noise from the sensor.

These conditions can introduce erroneous supervision signals when optimizing the parameters of the model. Suppose that one were to correctly identify the corresponding pixels between two images, the above nuisance factors would still cause the data-fidelity term of Eq. (1) to yield non-zero residuals, which induces gradients when backpropagating. Within the optimization of the weights θ , this update may translate to moving out of a local (possibly optimal) minima and result in performance degradations as shown in Fig. 1.

Thus, we propose an adaptive framework shown in Fig. 2 that incorporates a predictive correspondence scoring map to

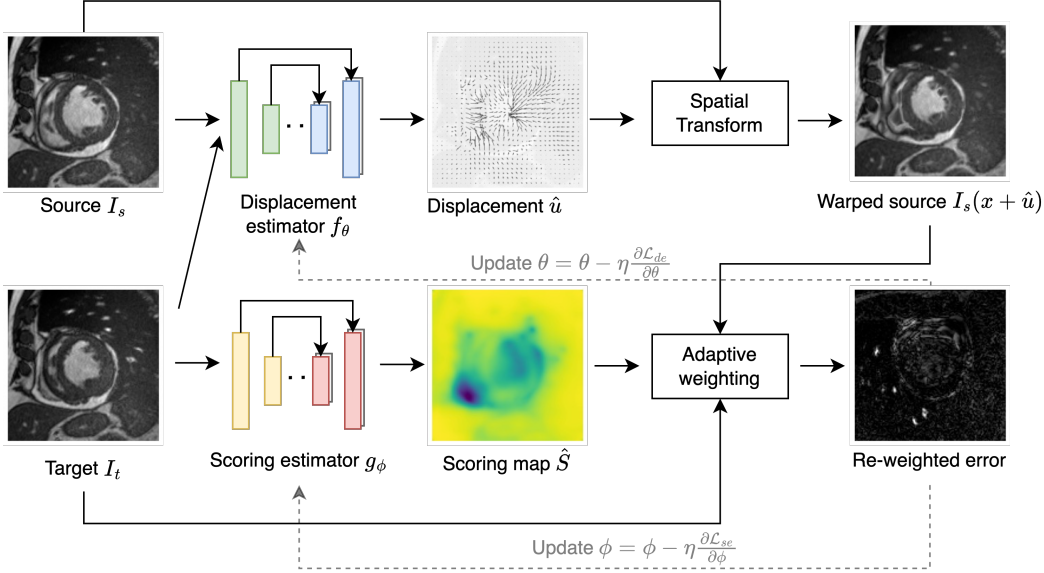


Figure 2. Diagram of training pipeline of our proposed adaptive scoring framework. Our proposed framework first estimates displacement \hat{u} from source and target image pair (I_s, I_t) . We then apply spatial transform to obtain the warped source image $I_s(x + \hat{u})$. Before computing error residuals, we estimate the correspondence scoring map from the target image I_t and then adaptively weight the error residuals for gradient-based optimization. The detailed training strategy is discussed in Algorithm 1.

prevent displacement estimation (de) from being dominated by error residuals due to nuisance variability. Our method is realized as an adaptive weighting term that can be generically integrated into the convention loss function for unsupervised training:

$$\mathcal{L}_{de} = \frac{1}{|\Omega|} \sum_{x \in \Omega} [\hat{S}(x)] \|I_t(x) - I_s(x + \hat{u}(x))\|_2^2 + \lambda \|\nabla \hat{u}(x)\|_2^2. \quad (2)$$

$\hat{S} : \Omega \rightarrow [0, 1]$ is a dense predictive pixel-wise scoring map to model the confidence score of how well one can establish correspondence between the two images, where higher values indicate a lower degree of effect from the nuisance variables (i.e. covisibility, noise, etc.). Note that this is equivalent to treating \hat{S} as the degree to which nuisance variables affect establishing correspondence between source and target images, and using its complement $1 - \hat{S}$. Floor symbol $\lfloor \cdot \rfloor$ denotes stop gradient operation.

4.2. Self-supervised correspondence scoring

The scoring estimator $g_\phi(\cdot)$ predicts a soft map to show the degree of correspondence existence from the target image as $\hat{S} = g_\phi(I_t)$. During training, the scoring estimator is optimized alternately with the displacement estimator $f_\theta(\cdot)$ under the following self-supervised correspondence scoring (scs) objective

$$\mathcal{L}_{scs} = \frac{1}{|\Omega|} \sum_{x \in \Omega} \hat{S}(x) \|I_t(x) - I_s(x + \lfloor \hat{u} \rfloor)\|_2^2. \quad (3)$$

Eq. (3) encourages the estimator to assign a lower score to regions with higher error residuals computed using the displacement estimated by $f_\theta(\cdot)$. However, minimizing Eq. (3) alone will lead to a degenerate solution where all scores are zeros. Thus, proper regularization is needed to prevent the estimator from such a solution.

4.3. Scoring estimator regularization

Given the range of the correspondence scoring map is $\hat{S}(x) \in [0, 1]$, we design the following objective by penalizing the degenerate solution of all zeros as a regularizer

$$\mathcal{L}_{reg} = \frac{1}{|\Omega|} \sum_{x \in \Omega} \|1 - \hat{S}(x)\|_2^2. \quad (4)$$

By having the above regularization alone, the scoring map will inevitably be non-smooth (e.g. flipping scoring between pixels) around neighboring regions that the model identifies as low correspondence during training. This is not desired since such non-smoothness will result in non-smooth displacement prediction when updating the displacement estimator parameters using Eq. (2), creating artifacts and distortion in image warping, and violating the assumption the local surfaces and structures are locally connected and smooth. Thus, having an additional smoothness constraint is essential to preserve such characteristics.

4.4. Momentum guided adaptive total variation

To impose smoothness regularization on the estimated correspondence scoring map, we introduce a momentum-guided adaptive weighting strategy that follows the training dynamics of the displacement estimator. In the early stage of training, the displacement estimator is largely in *exploration* phase, and thus both the predictions of displacement and scoring estimators are not accurate enough. Having strong smoothness regularization during this stage will harm the learning of both models. In the later stage of training, when both displacement and scoring estimators are close to convergence, the significance of the smoothness constraint intensifies to prevent non-smooth distortion when re-weighting error residuals.

To accommodate this design, we utilize the momentum of error residuals as an indicator of the current training status, adjusting the degree of the smoothness constraint accordingly. We first compute the mean of error residuals at the training step T as

$$\mu_T = \frac{1}{|\Omega|} \sum_{x \in \Omega} \|I_t(x) - I_s(x + [\hat{u}_T])\|_2^2. \quad (5)$$

Recall that $I_s(x), I_t(x) \in [0, 1]$, the mean error residuals are within range $\mu_T \in [0, 1]$. We then apply a cosine function that is monotonically decreasing concavely as the activation

$$b_T = \cos \frac{\pi}{2} \mu_T. \quad (6)$$

To compute the momentum of error residuals m_T , we apply the exponential moving average across different time steps with decay factor $\gamma = 0.99$ and $m_0 = 0$ as

$$m_T = \gamma m_{T-1} + (1 - \gamma) b_T. \quad (7)$$

We use the computed momentum $m_T \in [0, 1]$ as the adaptive weight to reflect the changes as training progresses along with the total variation as

$$\mathcal{L}_{\text{tv}} = m_T \frac{1}{|\Omega|} \sum_{x \in \Omega} \|\nabla \hat{S}(x)\|_2^2. \quad (8)$$

By having the scoring estimator during training, we prevent the displacement estimator from escaping local minima by re-weighting the error residuals with a smooth pixel-wise correspondence scoring, which leads to registration performance improvement. In order to exploit the characteristics of the displacement estimator and scoring estimator, a proper optimization strategy needs to be designed to ensure the effectiveness of the proposed adaptive framework, which is detailed in the following.

4.5. Optimization of proposed adaptive framework

We first define the final objective of the scoring estimator \mathcal{L}_{se} combining Eqs. (3), (4) and (8) as

$$\mathcal{L}_{\text{se}} = \mathcal{L}_{\text{scs}} + \alpha \mathcal{L}_{\text{reg}} + \beta \mathcal{L}_{\text{tv}} \quad (9)$$

with hyperparameter α and β to show the trade-off between different regularization.

To optimize displacement estimator $f_\theta(\cdot)$ and scoring estimator $g_\phi(\cdot)$ in training, we propose a collaborative strategy summarized in Algorithm 1. Since the parameter update of the displacement estimator and scoring estimator is correlated, as defined in Eq. (2) and Eq. (9), the noise in gradients tends to get exacerbated in the early stage of training when both estimators fail to provide each other an accurate prediction in order to properly optimize. To prevent this, we propose a warm-up stage that trains $f_\theta(\cdot)$ and $g_\phi(\cdot)$ individually for N_w epochs to reduce the error propagation in between. After the warm-up stage, we perform alternating optimization for both estimators.

Algorithm 1: Training loop

Data: Source image I_s and target image I_t
Result: Estimated displacement \hat{u}

- 1 Initialization, N_w : warm-up epochs, N : number of epochs;
- 2 **while** *epoch* i to N **do**
- 3 **if** $i < N_w$ **then**
- 4 flag_disp = True, flag_score = False;
- 5 **else if** $N_w \leq i < 2N_w$ **then**
- 6 flag_disp = False, flag_score = True;
- 7 **else**
- 8 flag_disp = True, flag_score = True;
- 9 **if** *flag_disp* **then**
- 10 $\hat{u} = f_\theta(I_s, I_t)$;
- 11 **if** *flag_score* **then**
- 12 $\hat{S} = g_\phi(I_s)$;
- 13 **else**
- 14 $\hat{S} = \mathbb{1}$;
- 15 $\theta = \theta - \eta \frac{\partial \mathcal{L}_{\text{de}}(I_s(x + \hat{u}), I_t, [\hat{S}])}{\partial \theta}$;
- 16 **if** *flag_score* **then**
- 17 $\hat{u} = f_\theta(I_s, I_t)$;
- 18 $\hat{S} = g_\phi(I_s)$;
- 19 $\phi = \phi - \eta \frac{\partial \mathcal{L}_{\text{se}}(I_s(x + [\hat{u}]), I_t, \hat{S})}{\partial \phi}$;

By training our proposed adaptive framework using the above optimization strategy summarized in Algorithm 1, we prevent the displacement estimator from drifting away from noisy gradients due to the nuisance variables such as covisibility and noise by re-weighting the error residuals using our adaptive correspondence scoring.

5. Experiments and details

5.1. Datasets

We tested our proposed framework on three different cardiac datasets, including two 2D public datasets, containing two medical imaging modalities (MRI and ultrasound), and one private 3D dataset. To construct the image pair, we selected the end-diastole (ED) frame as the source image and the end-systole (ES) frame as the target image. ED to ES registration is considered long-range and most challenging in the cardiac sequence. The detailed steps of dataset preprocessing can be found in the supplementary.

5.1.1 ACDC [5]

The ACDC dataset contains 2D human cardiac MRI from 150 patients with various cardiac conditions. We randomly selected 80 patients containing 751 image pairs for training, 20 patients containing 200 pairs for validation, and the remaining 50 patients containing 538 pairs for testing.

5.1.2 CAMUS [22]

The CAMUS dataset contains 2D human cardiac ultrasound images from 500 subjects. We randomly selected 600 image pairs for training, 200 pairs for validation, and another 200 pairs for testing.

5.1.3 Private 3D Echocardiography

To validate the effectiveness of our proposed method, we also tested on a private 3D echocardiography dataset and reported our results in the supplementary.

5.2. Evaluation metrics

We evaluate our results quantitatively by warping myocardium segmentation in the source image with our predicted displacement vector \hat{u} and compute anatomical conformance in terms of 1) Dice coefficient score (DSC) 2) Hausdorff distance (HD) and 3) Average surface distance (ASD) with ground truth segmentation in the target image.

5.3. Implementation details

All our experiments were implemented using Pytorch on NVIDIA V100/A5000 GPUs. The architecture of the scoring estimator is implemented on a U-Net backbone. To show the versatility of our proposed framework, we tested on three representative unsupervised registration architectures for each dataset: 1) Voxelmorph [4], 2) Transmorph [7] and 3) Diffusemorph [20]. The details of other baselines are summarized in the following:

5.3.1 Adaptive weighting schemes

AdaReg [32] At each step, we compute first the local error residual $\rho = |I_t(x) - I_s(x + \hat{u})|$ and the global residual $\sigma = \frac{1}{|\Omega|} \sum_{x \in \Omega} |I_t(x) - I_s(x + \hat{u})|$ using the displacement estimator prediction \hat{u} . We then compute the adaptive regularization weighting as $\alpha(x) = \exp(-\frac{\rho}{\sigma})$, where $c = 50$. We then optimize the displacement estimator using the loss $\mathcal{L}_{\text{AdaReg}} = \frac{1}{|\Omega|} \sum_{x \in \Omega} \|I_t(x) - I_s(x + \hat{u})\|_2^2 + \lambda \|\alpha(x) \nabla \hat{u}\|_2^2$.

AdaFrame [33] At each step, we first compute the local error residual $\delta = |I_t(x) - I_s(x + \hat{u})|$ and then normalize it with its mean μ and standard deviation σ as $\rho = \frac{\delta - \mu}{\sqrt{\sigma^2 + \epsilon}}$. We then compute the adaptive weight activated by a scaled and shifted sigmoid function as $\alpha(x) = 1 - \frac{1}{1 + \exp(-\frac{1}{(a\rho - b)})}$ where $a = \frac{a_0}{\mu + \epsilon}$ and $b = b_0(1 - \cos \pi \mu)$. We choose $a_0 = 0.1$ and $b_0 = 10$. We then optimize the displacement estimator using the loss $\mathcal{L}_{\text{AdaFrame}} = \frac{1}{|\Omega|} \sum_{x \in \Omega} \alpha(x) \|I_t(x) - I_s(x + \hat{u})\|_2^2 + \lambda \|\nabla \hat{u}\|_2^2$.

5.3.2 Aleatoric uncertainty estimation

In order to obtain the predictive variance, we utilize a U-Net as variance estimator $h(\cdot)$ that takes target image I_t and warped source $I_s(x + \hat{u})$ as input to predict the noise variance $\hat{\sigma}_I = h(I_t, I_s(x + \hat{u}))$. The variance estimator is trained jointly with displacement estimator.

NLL [19] To jointly train the displacement and variance estimators under the NLL objective, we compute the loss as $\mathcal{L}_{\text{NLL}} = \frac{1}{|\Omega|} \sum_{x \in \Omega} \frac{1}{\hat{\sigma}_I^2(x)} \|I_t(x) - I_s(x + \hat{u})\|_2^2 + \log \hat{\sigma}_I^2(x)$

β -NLL [29] To jointly train the displacement and variance estimators under β -NLL objective, we compute the loss as $\mathcal{L}_{\beta\text{-NLL}} = \frac{1}{|\Omega|} \sum_{x \in \Omega} [\hat{\sigma}_I(x)^{2\beta}] \left(\frac{1}{\hat{\sigma}_I^2(x)} \|I_t(x) - I_s(x + \hat{u})\|_2^2 + \log \hat{\sigma}_I^2(x) \right)$ where $\beta = 0.5$.

The remaining details including hyperparameter selection can be found in the supplementary.

6. Results

6.1. Registration accuracy

We present our quantitative evaluation in Tab. 1. From the table, our proposed method shows consistent improvement over other baselines. Compared to Voxelmorph [4], Transmorph [7], and Diffusemorph [20], which are the second-best methods in each architecture, our proposed method performs better especially in terms of Dice score on each dataset.

We additionally conducted a paired t-test of our proposed method to show that our consistent improvement is statistically significant as in Tab. 2.

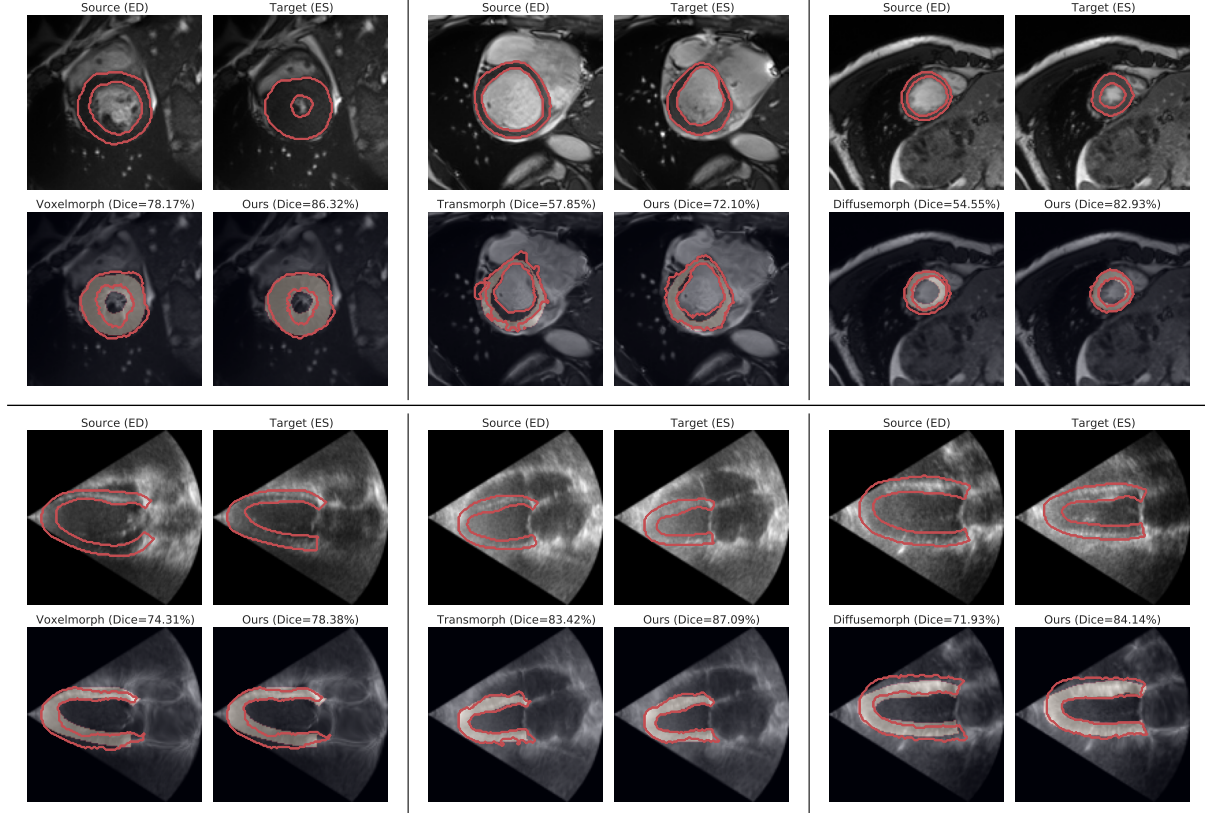


Figure 3. Quantitative evaluation of our method against the second-best approach in each dataset (top two rows: ACDC [5] and bottom two rows: CAMUS [20]). Each block, delineated by black solid lines, features source and target images with myocardium segmentation contours. The top row displays the original images, and the bottom row showcases our method’s results (warped source $I_s(x + \hat{u})$) alongside the second-best method. The yellow background indicates the ground truth ES myocardium. Dice scores are reported in the subtitles.

		ACDC [5]			CAMUS [22]		
		DSC \uparrow	HD \downarrow	ASD \downarrow	DSC \uparrow	HD \downarrow	ASD \downarrow
CNN	Voxelmorph [4]	79.48	4.79	1.27	81.50	8.72	1.74
	NLL [19]	76.49	5.46	1.45	75.24	11.05	2.20
	β -NLL [29]	78.74	5.07	1.33	79.75	9.39	1.93
	AdaFrame [33]	66.38	5.80	1.67	77.88	10.54	1.93
	AdaReg [32]	78.75	5.13	1.33	79.31	9.78	1.88
	AdaCS (Ours)	80.50	4.69	1.23	81.74	8.55	1.72
Transformer	Transmorph [7]	76.94	5.51	1.30	79.24	10.30	1.79
	NLL [19]	73.12	7.22	1.27	75.08	11.60	1.79
	β -NLL [29]	75.74	6.12	1.29	77.39	10.99	1.86
	AdaFrame [33]	67.95	5.72	1.59	78.06	9.86	1.91
	AdaReg [32]	76.22	5.68	1.29	78.12	10.62	1.84
	AdaCS (Ours)	78.39	5.40	1.32	79.64	9.85	1.79
Diffusion	Diffusemorph [20]	67.38	5.80	1.67	75.23	9.80	2.07
	NLL [19]	66.24	5.84	1.73	74.78	10.62	2.15
	β -NLL [29]	66.31	5.93	1.74	73.27	9.85	2.25
	AdaFrame [33]	59.78	6.46	1.93	75.04	10.41	2.10
	AdaReg [32]	69.41	6.25	1.78	74.36	10.66	2.21
	AdaCS (Ours)	72.09	5.35	1.53	77.65	9.82	1.99

Table 1. Contour-based metrics compared against baselines. Units: DSC (%) HD (vx) ASD (vx). Our method consistently improves on registration accuracy across different architectures and datasets.

To quantitatively evaluate the registration performance,

	Voxelmorph [4]	Transmorph [7]	Diffusemorph [20]
ACDC [5]	$p < 0.05$	$p < 0.05$	$p < 0.05$
CAMUS [22]	$p < 0.05$	$p < 0.05$	$p < 0.05$

Table 2. Paired t-test of our proposed method v.s. second-best method in Tab. 1 for each dataset in terms of DSC. The p-values suggested that our improvement is statistically significant.

we plot the warped source image along with segmentation overlaid with ground truth shown in Fig. 3. Our proposed framework is visually better across datasets with different modalities and frameworks. Both the quantitative and qualitative evaluations show that our proposed framework captures more accurate correspondence, validating the effectiveness of our proposed adaptive scoring.

From Tab. 1, we note that both uncertainty weighting strategies, NLL [19] and β -NLL [29], did not yield improvements over the baseline. This observation indicates that optimization of uncertainty estimation cannot be approached with a simple joint optimization alongside image registration. Furthermore, we observe that adaptive regularization techniques, exemplified by AdaFrame [33] and AdaReg [32],

were ineffective in enhancing performance, which could be attributed to the computation of adaptive weights based on statistical assumptions of error residuals contrary to our proposed self-supervised learning approach. Additionally, a discernible decline in performance is noted when transitioning from Voxelmorph [4], which utilizes ConvNets, to Transmorph [7] and Diffusemorph [20]. This decline underscores the challenges faced by transformer and diffusion-based models when applied to datasets comprising smaller-scale medical images.

6.2. Qualitative results of correspondence scoring map and adaptive weight

To qualitatively evaluate the effectiveness of our proposed correspondence scoring during training, we present Fig. 4 to show that our predicted scoring map accurately identifies the regions with low correspondence and prevents the displacement estimator $f_{\theta}(\cdot)$ from drifting away by re-weighting the error residuals with our map.

In Fig. 5, we illustrate the behavior of our proposed adaptive momentum-guided weight, denoted as m_T (Eq. (7)). This weight dynamically adapts during training, responding to the evolving characteristics of error residuals (Eq. (5)). The observed evolution of our adaptive weight aligns with our design objective, progressively enhancing smoothness penalization as training toward convergence.

6.3. Ablation study

We present Tab. 3 for ablation studies to show the effectiveness of each loss term. Without \mathcal{L}_{reg} and \mathcal{L}_{tv} , the predicted correspondence scoring map \hat{S} will result in a degenerate solution of all zeros. By introducing regularization and smoothness constraints, the performance of our proposed framework steadily increases across various datasets and registration architectures.

	Loss		ACDC [5]			CAMUS [22]		
	\mathcal{L}_{reg}	\mathcal{L}_{tv}	DSC \uparrow	HD \downarrow	ASD \downarrow	DSC \uparrow	HD \downarrow	ASD \downarrow
vxm	✓	✗	80.24	4.64	1.23	81.58	8.89	1.74
	✓	✓	80.50	4.69	1.23	81.74	8.55	1.72
tsm	✓	✗	77.84	5.41	1.33	79.58	10.17	1.81
	✓	✓	78.39	5.40	1.32	79.64	9.85	1.79
dfm	✓	✗	71.62	5.56	1.58	77.32	9.71	2.00
	✓	✓	72.09	5.35	1.53	77.65	9.82	1.99

Table 3. Ablation study on loss terms. Note: Removing \mathcal{L}_{reg} leads to a degenerate solution of all-zeros for the scoring estimator $g_{\phi}(\cdot)$.

7. Conclusion

In this paper, we propose an adaptive correspondence scoring framework for unsupervised image registration to prevent

the displacement estimator from drifting away by noisy gradients caused by low correspondence due to the nuisance variables such as noise or covisibility during training. We introduce a self-supervised correspondence scoring estimation scheme with both scoring and momentum-guided adaptive regularizations to prevent the scoring estimator from a degenerate solution and ensure scoring map smoothness. We demonstrate the effectiveness of our proposed framework on three representative registration architectures and we show consistent improvement compared with other baselines across three medical image datasets with diverse modalities. Though our proposed framework is promising, the hyperparameters in the scoring estimator loss need to be tuned for each architecture on each dataset. In the future, we aim to explore an amortized hyperparameter optimization scheme during training to reduce the computation and validate our proposed framework on clinical datasets for further impact.

8. Acknowledgement

This work is supported by NIH grant R01HL121226.

References

- [1] John Ashburner. A fast diffeomorphic image registration algorithm. *NeuroImage*, 38(1):95–113, 2007. 1
- [2] B. B. Avants, C. L. Epstein, M. Grossman, and J. C. Gee. Symmetric diffeomorphic image registration with cross-correlation: Evaluating automated labeling of elderly and neurodegenerative brain. *Medical Image Analysis*, 12(1): 26–41, 2008. 1
- [3] Gwangbin Bae, Ignas Budvytis, and Roberto Cipolla. Estimating and Exploiting the Aleatoric Uncertainty in Surface Normal Estimation. In *2021 IEEE/CVF International Conference on Computer Vision (ICCV)*, pages 13117–13126, Montreal, QC, Canada, 2021. IEEE. 3
- [4] Guha Balakrishnan, Amy Zhao, Mert R. Sabuncu, John Guttag, and Adrian V. Dalca. VoxelMorph: A Learning Framework for Deformable Medical Image Registration. *IEEE Transactions on Medical Imaging*, 38(8):1788–1800, 2019. 1, 2, 3, 6, 7, 8, 9
- [5] Olivier Bernard, Alain Lalonde, Clement Zotti, Frederick Cervenansky, Xin Yang, Pheng-Ann Heng, Irem Cetin, Karim Lekadir, Oscar Camara, Miguel Angel Gonzalez Ballester, Gerard Sanroma, Sandy Napel, Steffen Petersen, Georgios Tziritas, Elias Grinias, Mahendra Khened, Varghese Alex Kollerathu, Ganapathy Krishnamurthi, Marc-Michel Rohe, Xavier Pennec, Maxime Sermesant, Fabian Isensee, Paul Jager, Klaus H. Maier-Hein, Peter M. Full, Ivo Wolf, Sandy Engelhardt, Christian F. Baumgartner, Lisa M. Koch, Jelmer M. Wolterink, Ivana Isgum, Yeonggul Jang, Yoonmi Hong, Jay Patravali, Shubham Jain, Olivier Humbert, and Pierre-Marc Jodoin. Deep Learning Techniques for Automatic MRI Cardiac Multi-Structures Segmentation and Diagnosis: Is the Problem Solved? *IEEE Transactions on Medical Imaging*, 37(11):2514–2525, 2018. 2, 6, 7, 8, 9, 1

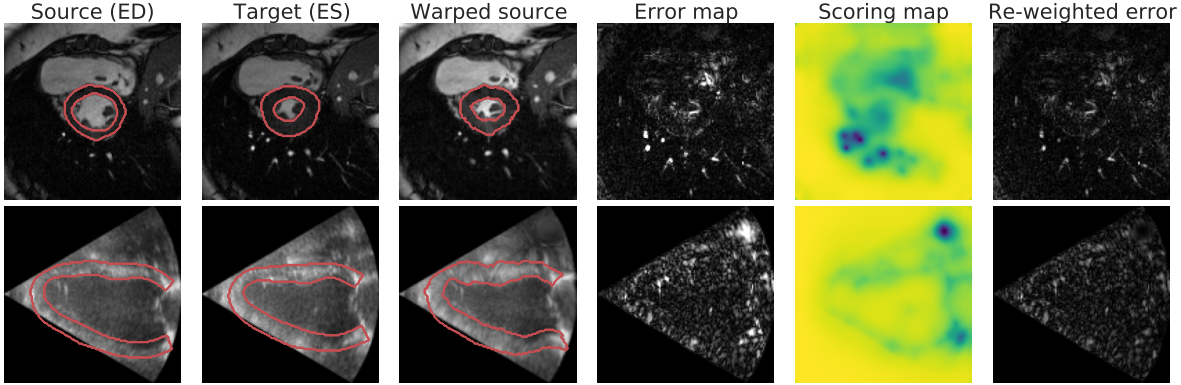


Figure 4. Qualitative visualization of our proposed framework in Voxelmorph architecture [4] on ACDC [5] (top row) and CAMUS [22] (bottom row) validation sets. The third column exhibits successful matching, but the error map in the fourth column reveals residuals. Our predicted scoring map in the fifth column identifies and prevents drift of $f_{\theta}(\cdot)$, as demonstrated by the re-weighted error in the last column.

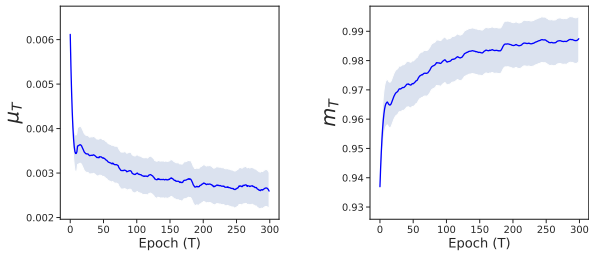


Figure 5. Left: Mean of error residuals μ_T defined in Eq. (5). Right: Adaptive momentum guided weight m_T defined in Eq. (7).

[6] Jieneng Chen, Yongyi Lu, Qihang Yu, Xiangde Luo, Ehsan Adeli, Yan Wang, Le Lu, Alan L. Yuille, and Yuyin Zhou. TransUNet: Transformers Make Strong Encoders for Medical Image Segmentation, 2021. arXiv:2102.04306 [cs]. 2

[7] Junyu Chen, Eric C. Frey, Yufan He, William P. Segars, Ye Li, and Yong Du. TransMorph: Transformer for unsupervised medical image registration. *Medical Image Analysis*, 82: 102615, 2022. 1, 2, 3, 6, 7, 8

[8] Adrian V. Dalca, Guha Balakrishnan, John Guttag, and Mert R. Sabuncu. Unsupervised Learning for Fast Probabilistic Diffeomorphic Registration. pages 729–738. 2018. arXiv:1805.04605 [cs]. 1

[9] Adrian V. Dalca, Guha Balakrishnan, John Guttag, and Mert R. Sabuncu. Unsupervised learning of probabilistic diffeomorphic registration for images and surfaces. *Medical Image Analysis*, 57:226–236, 2019. 2

[10] Christos Davatzikos. Spatial Transformation and Registration of Brain Images Using Elastically Deformable Models. *Computer Vision and Image Understanding*, 66(2):207–222, 1997. 1

[11] Alexey Dosovitskiy, Lucas Beyer, Alexander Kolesnikov, Dirk Weissenborn, Xiaohua Zhai, Thomas Unterthiner, Mostafa Dehghani, Matthias Minderer, Georg Heigold, Sylvain Gelly, Jakob Uszkoreit, and Neil Houlsby. An Image is

Worth 16x16 Words: Transformers for Image Recognition at Scale, 2021. arXiv:2010.11929 [cs]. 2

[12] Derek L G Hill, Philipp G Batchelor, Mark Holden, and David J Hawkes. Medical image registration. 1

[13] Malte Hoffmann, Benjamin Billot, Douglas N. Greve, Juan Eugenio Iglesias, Bruce Fischl, and Adrian V. Dalca. SynthMorph: learning contrast-invariant registration without acquired images. *IEEE Transactions on Medical Imaging*, 41(3):543–558, 2022. arXiv:2004.10282 [cs, eess, q-bio]. 2

[14] Byung-Woo Hong, Ja-Keoung Koo, Martin Burger, and Stefano Soatto. Adaptive Regularization of Some Inverse Problems in Image Analysis, 2017. arXiv:1705.03350 [cs]. 3

[15] Byung-Woo Hong, Ja-Keoung Koo, Hendrik Dirks, and Martin Burger. Adaptive Regularization in Convex Composite Optimization for Variational Imaging Problems, 2017. arXiv:1609.02356 [cs]. 3

[16] Andrew Hoopes, Malte Hoffmann, Bruce Fischl, John Guttag, and Adrian V. Dalca. HyperMorph: Amortized Hyperparameter Learning for Image Registration, 2021. arXiv:2101.01035 [cs, eess]. 2

[17] Eyke Hüllermeier and Willem Waegeman. Aleatoric and epistemic uncertainty in machine learning: an introduction to concepts and methods. *Machine Learning*, 110(3):457–506, 2021. 3

[18] Robert Keelan, Kenji Shimada, and Yoed Rabin. GPU-Based Simulation of Ultrasound Imaging Artifacts for Cryosurgery Training. *Technology in Cancer Research & Treatment*, 16(1):5–14, 2017. Publisher: SAGE Publications Inc. 3

[19] Alex Kendall and Yarin Gal. What Uncertainties Do We Need in Bayesian Deep Learning for Computer Vision?, 2017. arXiv:1703.04977 [cs]. 3, 6, 7, 1

[20] Boah Kim, Inhwa Han, and Jong Chul Ye. DiffuseMorph: Unsupervised Deformable Image Registration Using Diffusion Model. In *Computer Vision – ECCV 2022*, pages 347–364, Cham, 2022. Springer Nature Switzerland. 1, 2, 3, 6, 7, 8

[21] S. Klein, M. Staring, K. Murphy, M.A. Viergever, and J. Pluim. elastix: A Toolbox for Intensity-Based Medical Image Registration. *IEEE Transactions on Medical Imaging*, 29(1): 196–205, 2010. 1

- [22] Sarah Leclerc, Erik Smistad, Joao Pedrosa, Andreas Ostvik, Frederic Cervenansky, Florian Espinosa, Torvald Espeland, Erik Andreas Rye Berg, Pierre-Marc Jodoin, Thomas Grenier, Carole Lartizien, Jan Dhooge, Lasse Lovstakken, and Olivier Bernard. Deep Learning for Segmentation Using an Open Large-Scale Dataset in 2D Echocardiography. *IEEE Transactions on Medical Imaging*, 38(9):2198–2210, 2019. 2, 6, 7, 8, 9, 1
- [23] Ze Liu, Yutong Lin, Yue Cao, Han Hu, Yixuan Wei, Zheng Zhang, Stephen Lin, and Baining Guo. Swin Transformer: Hierarchical Vision Transformer Using Shifted Windows. pages 10012–10022, 2021. 2
- [24] Tai Ma, Xinru Dai, Suwei Zhang, and Ying Wen. PIViT: Large Deformation Image Registration with Pyramid-Iterative Vision Transformer. In *Medical Image Computing and Computer Assisted Intervention – MICCAI 2023*, pages 602–612, Cham, 2023. Springer Nature Switzerland. 3
- [25] Miguel Monteiro, Loic Le Folgoc, Daniel Coelho de Castro, Nick Pawlowski, Bernardo Marques, Konstantinos Kamnitsas, Mark van der Wilk, and Ben Glocker. Stochastic Segmentation Networks: Modelling Spatially Correlated Aleatoric Uncertainty. In *Advances in Neural Information Processing Systems*, pages 12756–12767. Curran Associates, Inc., 2020. 3
- [26] Francisco P M Oliveira. Medical Image Registration: a Review. 1
- [27] Yi Qin and Xiaomeng Li. FSDiffReg: Feature-wise and Score-wise Diffusion-guided Unsupervised Deformable Image Registration for Cardiac Images, 2023. arXiv:2307.12035 [cs]. 3
- [28] D. Rueckert, L.I. Sonoda, C. Hayes, D.L.G. Hill, M.O. Leach, and D.J. Hawkes. Nonrigid registration using free-form deformations: application to breast MR images. *IEEE Transactions on Medical Imaging*, 18(8):712–721, 1999. 1
- [29] Maximilian Seitzer, Arash Tavakoli, Dimitrije Antic, and Georg Martius. On the Pitfalls of Heteroscedastic Uncertainty Estimation with Probabilistic Neural Networks, 2022. arXiv:2203.09168 [cs, stat]. 3, 6, 7, 1
- [30] Jiacheng Shi, Yuting He, Youyong Kong, Jean-Louis Coatrieux, Huazhong Shu, Guanyu Yang, and Shuo Li. XMorpher: Full Transformer for Deformable Medical Image Registration via Cross Attention, 2022. arXiv:2206.07349 [cs]. 1, 3
- [31] Jiaming Song, Chenlin Meng, and Stefano Ermon. Denoising Diffusion Implicit Models, 2022. arXiv:2010.02502 [cs]. 3
- [32] Alex Wong and Stefano Soatto. Bilateral Cyclic Constraint and Adaptive Regularization for Unsupervised Monocular Depth Prediction. In *2019 IEEE/CVF Conference on Computer Vision and Pattern Recognition (CVPR)*, pages 5637–5646, Long Beach, CA, USA, 2019. IEEE. 3, 6, 7, 1
- [33] Alex Wong, Xiaohan Fei, Byung-Woo Hong, and Stefano Soatto. An Adaptive Framework for Learning Unsupervised Depth Completion. *IEEE Robotics and Automation Letters*, 6(2):3120–3127, 2021. 3, 6, 7, 1
- [34] Xiaoran Zhang, Chenyu You, Shawn Ahn, Juntang Zhuang, Lawrence Staib, and James Duncan. Learning Correspondences of Cardiac Motion from Images Using Biomechanics-Informed Modeling. In *Statistical Atlases and Computational*

Models of the Heart. Regular and CMRxMotion Challenge Papers, pages 13–25, Cham, 2022. Springer Nature Switzerland. 1

An Adaptive Correspondence Scoring Framework for Unsupervised Image Registration of Medical Images

Supplementary Material

9. Dataset details

9.1. ACDC [5]

The ACDC dataset, publicly accessible, comprises 2D cardiac MRI scans from 150 patients, with 100 subjects allocated for training and 50 for testing. Each sequence includes frames at end-diastole (ED) and end-systole (ES), along with corresponding myocardium labels. Our training set involves 80 randomly selected patients, the validation set consists of 20 patients, and the testing set comprises 50 patients. Extracting ED and ES image pairs is done in a slice-by-slice manner from the 2D longitudinal stacks. We perform a center crop for each slice pair, resulting in dimensions of 128×128 with respect to the myocardium centroid in the ED frame. This process yields a total of 751 2D image pairs for training, 200 pairs for validation, and an additional 538 pairs for testing.

9.2. CAMUS [22]

The CAMUS dataset, available to the public, comprises 2D cardiac ultrasound images from 500 individuals. Each individual contributes two distinct images: one for a 2-chamber view and another for a 4-chamber view. For every image, both end-diastole (ED) and end-systole (ES) frames, along with myocardium segmentation labels, are provided. We crop each image pair to 128×128 , and through random selection, we use 300 subjects for training, 100 subjects for validation, and 100 subjects for testing. This process results in a total of 600 2D image pairs for training, 200 pairs for validation, and an additional 200 pairs for testing.

9.3. Private 3D Echo

The private 3D echo dataset contains 99 cardiac ultrasound scans with 8 sequences from synthetic ultrasound, 40 sequences from *in vivo* canine, and another 51 sequences from *in vivo* porcine. The details of the acquisition are omitted to preserve anonymity in the review process. ED and ES frames are manually identified and myocardium segmentation labels are provided for each sequence by experienced radiologists. Each 3D image is resized to $64 \times 64 \times 64$ during training. We randomly selected 60 3D pairs for training, 19 pairs for validation, and another 20 pairs for testing. During testing, the estimated displacement is resized and rescaled to the original volume dimension and we compute anatomical scores of warped and target myocardium volumes afterwards.

10. Hyperparameter tuning

To optimize the hyperparameters in our proposed framework (α for scoring estimator regularization and β for momentum-guided adaptive total variation defined in Eq. (9)), we utilize the strategy of tuning one parameter at a time. We first optimize α through grid search with $\beta = 0$. We then optimize β with a fixed α from the previous experiments. This process needs to be repeated for each architecture under each dataset.

11. Additional results on private 3D Echo

We present our qualitative result on the private 3D Echo dataset across three architectures with Fig. 6, where we show that our proposed framework achieves a better registration accuracy evidenced by better matching with the ground truth (yellow overlaid), smoother contour edges and locally consistent myocardial regions. We further show our quantitative results with Tab. 4, where our proposed framework outperforms other baselines on Voxelmorph and Diffusemorph architectures with comparable performance with the vanilla version on Transmorph architecture. This might be due to that the testing size of our private 3D Echo dataset is small with only 20 cases, which we aim to further evaluate on larger *in vivo* animal datasets.

		Private 3D Echo		
		DSC \uparrow	HD \downarrow	ASD \downarrow
CNN	Voxelmorph [4]	77.23	16.27	2.14
	NLL [19]	75.58	18.02	3.11
	β -NLL [29]	76.80	16.78	2.88
	AdaFrame [33]	76.66	16.25	2.11
	AdaReg [32]	76.28	17.41	2.17
	AdaCS (Ours)	77.33	16.36	2.13
Transformer	Transmorph [7]	74.89	17.45	2.14
	NLL [19]	70.56	19.60	2.00
	β -NLL [29]	71.98	17.96	2.15
	AdaFrame [33]	75.57	17.30	2.18
	AdaReg [32]	74.39	18.14	2.13
	AdaCS (Ours)	75.54	17.30	2.16
Diffusion	Diffusemorph [20]	73.56	16.51	2.40
	NLL [19]	70.36	17.81	2.50
	β -NLL [29]	69.38	17.13	2.54
	AdaFrame [33]	71.47	16.57	2.39
	AdaReg [32]	73.32	17.75	2.38
	AdaCS (Ours)	73.91	16.74	2.39

Table 4. Contour-based metrics compared against baselines on our private 3D Echo dataset. DSC (%), HD (vx), ASD (vx).

We additionally show the qualitative result of the adaptive

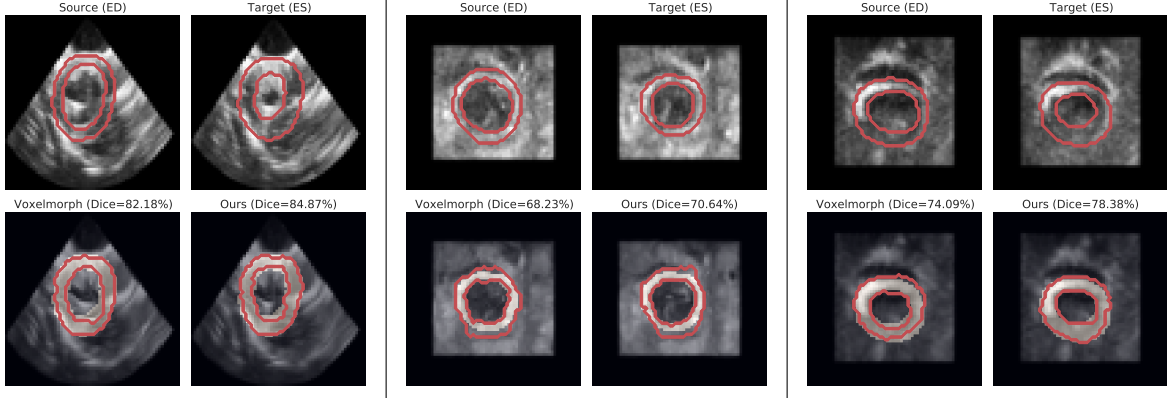


Figure 6. Quantitative evaluation of our method against the second-best approach on our private 3D Echo dataset. Cross-sectional slices are extracted from the 3D volumes for visualization. Each block, delineated by black solid lines, features source and target images with myocardium segmentation contours. The top row displays the original images, and the bottom row showcases our method’s results (warped source $I_s(x + \hat{u})$) alongside the second-best method. The yellow background indicates the ground truth ES myocardium. Dice scores are reported in the subtitles.

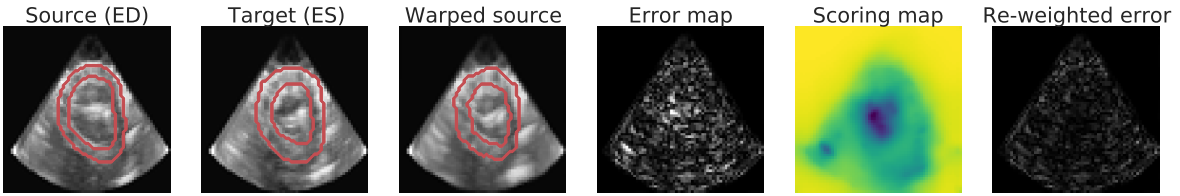


Figure 7. Qualitative visualization of our proposed framework in VoxelMorph architecture [4] on our private 3D Echo validation sets. Cross-sectional slices are extracted from the 3D volumes for visualization. The third column exhibits successful matching, but the error map in the fourth column reveals residuals. Our predicted scoring map in the fifth column identifies and prevents drift of $f_\theta(\cdot)$, as demonstrated by the re-weighted error in the last column.

scoring map on 3D private Echo with Fig. 7 during training. Cross-sectional slices are extracted from the 3D volumes for visualization. We show that our proposed scoring map in the fifth column is able to identify regions with loss of correspondence (e.g. by comparing regions in the first two columns) and adaptive re-weight the error residuals to prevent the displacement estimator from being driven away by the spurious error residuals, leading to performance improvement, consistent to our finding in Sec. 6.2.